Nano Research

Open Access

Communication

Unconventional orthorhombic-phase graphite in Cretaceous foraminiferal fossils

Qingyi Sheng ✉ and Yiwei Xu

State Key Laboratory of Palaeobiology and Stratigraphy, Nanjing Institute of Geology and Palaeontology, Chinese Academy of Sciences, Nanjing 210008, China

Cite this article: *Nano Research*, **2025**, *18*, 94907262. https://doi.org/10.26599/NR.2025.94907262

ABSTRACT: Fossils serve as faithful records and indicators of past geological events. However, accurately identifying organic remnants in these specimens remains challenging due to long-term degradation and transformation processes. In this study, we characterized Cretaceous foraminiferal fossils from different stratigraphic layers using optical microscopy, X-ray diffraction (XRD), scanning electron microscopy (SEM), energy-dispersive X-ray spectroscopy (EDS), and Raman spectroscopy. Our analyses reveal an unconventional orthorhombic phase of graphite in some samples, suggesting exposure to extreme conditions—such as high temperature and high pressure—during the mid-Cretaceous. These findings not only provide valuable insights into the geological history of that period but also offer a promising avenue for understanding the chemical synthesis of novel carbon materials through polymorphic transformations.

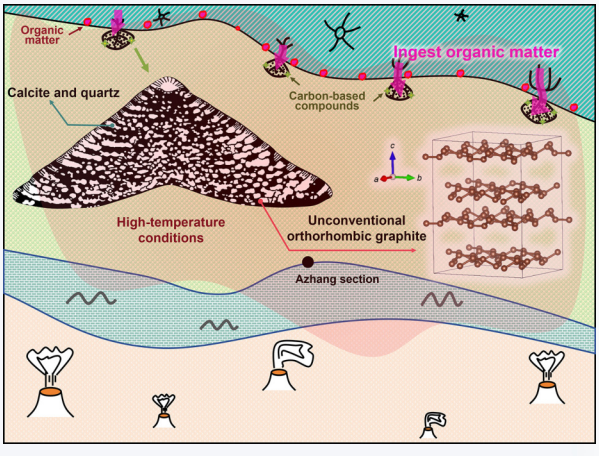

KEYWORDS: foraminifera, orthorhombic, graphite, Cretaceous, polymorph

1 Introduction

Fossils are faithful recorders and indicators of geological history and events, providing insights through their spatial and compositional structures [1–3]. Foraminifera [4–7], a typical group of Protozoa, have persisted from the Late Ediacaran to the present [8–10]. Thus, foraminifera can act as descriptors [11] for biological evolution and advanced taxonomic relationships over a long period of geologic time and a wide range of localities [12–15].

The Cretaceous period [16] is marked by significant evolutionary and geological transitions. In particular, the mid-Cretaceous (approximately 125–90 million years ago) experienced widespread volcanic activity, including the formation of large igneous provinces (LIPs). These volcanic events released massive amounts of carbon dioxide (CO_2) into the atmosphere [17–22], contributing to greenhouse warming [17, 23, 24] and significant oceanic anoxic events (OAEs) [16]. These OAEs led to extensive organic carbon burial in marine sediments and significant perturbations to the global carbon cycle. Volcanism during this time not only shaped the Earth's climate but also influenced the preservation and transformation of organic materials in geological formations.

The findings from fossil indicators are critical but often challenging to interpret. This difficulty arises because the preservation of organic compounds [25, 26] and minute crystallites [27] varies significantly over millions of years. Moreover, the chemical transformation of these components is quite complex, leaving elusive remnants in the fossils [28, 29].

In this work, we study two sets of samples collected from the Cretaceous period. Despite the similar components of calcite and quartz, both in the mineral matrix and inside the foraminifera, we find that the components of carbon deposits in these two samples exhibit substantial differences. This indicates that the organic components in the foraminifera underwent distinct pathways during burial and fossilization. Comprehensive characterization using powder X-ray diffraction (XRD), scanning electron microscopy (SEM), energy-dispersive X-ray spectroscopy (EDS) and Raman spectroscopy reveals that high-temperature and high-pressure events, likely related to mid-Cretaceous volcanic activity, affected one of the samples, leading to a thermally unstable, unconventional orthorhombic phase of graphite. Our findings not

Received: January 6, 2025; **Revised:** January 15, 2025
Accepted: January 17, 2025

✉Address correspondence to qysheng@nigpas.ac.cn

only provide insights into the geological events of the mid-Cretaceous but also shed light on chemical scientists who seek new polymorphs of carbon materials.

2 Experimental details

The XRD patterns of the Cretaceous specimens were collected on a German Bruker D8 Advance diffractometer powder diffractometer, Cu Kα ray (λ = 1.54056 Å; 40 kV; 40 mA). The step size is 0.015° and the data collection angle is from 10° to 80°. All data were collected at ambient atmosphere and temperature. The SEM imaging was performed using a JEOL JSM-IT500HR, with EDS (Oxford Instrument). The Raman spectra were obtained using a Raman microscope (Thermo Fischer DXR) with a laser at 532 nm.

To investigate the interactions between valence electrons and atomic nuclei, the projector augmented wave (PAW) method was utilized. The density functional theory (DFT) calculation: To investigate the interactions between valence electrons and atomic nuclei, the PAW [30] method was utilized. For the evaluation of electron exchange-correlation interactions, the generalized gradient approximation (GGA) [31] of Perdew–Burke–Ernzerhof (PBE) [31] was employed. To ensure accurate total energy calculations for both the orthorhombic and hexagonal graphite systems, a plane wave energy cutoff of 400 eV was set, and a convergence threshold of 10^{-5} eV/atom was used. For reciprocal space sampling, a 6 × 6 × 4 k-point grid was adopted, and the Monkhorst–Pack method was applied during the self-consistent field iterations.

3 Results and discussion

The foraminiferal samples we studied in this work are collected from the Aptian stage (K1 sample), and the Cenomanian stage (K2 sample) of the Langshan Formation at the Azhang section. The large benthic foraminifera orbitolininids [32] are abundant in samples and suitable for research. Thick carbonate sequences, named the Langshan Formation were accumulated in the northern Lhasa block during the mid-Cretaceous [33, 34] (Fig. 1(a)). The Langshan Formation conformably overlies clastic rocks and has a depositional age ranging from early Aptian to middle Cenomanian based on biostratigraphy [33–36]. In the Azhang section (Fig. 1(b)), the Langshan Formation can be subdivided into three informal members based on lithology. Member 1 and Member 3 comprise shallow water massive bioclastic limestone with abundant rudists, green algae, big benthic foraminifers such as orbitolinids, and other smaller benthic foraminifers [33, 36]. Member 2 comprises open marine marlstones with planktonic foraminifers and calcispheres [33, 36]. The K1 sample was collected from the Member 1, and the K2 sample was collected from the Member 3.

The K1 and K2 samples exhibit distinct microstructures. First of all, the XRD analysis [38] can reveal all the inorganic crystalline phases in the foraminiferal fossils. In the XRD pattern (Fig. 2(a)) of the K1 specimen, the crystallite of calcite ($CaCO_3$), quartz (SiO_2) and graphite (C) can be clearly found and indexed. We further conducted Rietveld refinement [39–41] to unveil the relative content of each mineral. The result shows that the weight fractions of calcite ($CaCO_3$), quartz (SiO_2) and graphite (C) are 93.70%, 3.27% and 3.03%, respectively. The lattice parameters are listed below. The calcite ($CaCO_3$) belongs to the space group of *R*3*c* and a hexagonal system [42], with a = 4.97 Å and c = 17.00 Å. Quartz (SiO_2) is assigned as a space group of $P3_121$ and a hexagonal system [43], with a = 4.90 Å and c = 5.39 Å. The unconventional phase of graphite belongs to the space group of Pban and an orthorhombic system [44], with a = 3.90 Å, b = 4.88 Å and c = 6.39 Å. We then also carried out XRD analysis on the K2 specimen and found only the existence of calcite ($CaCO_3$) and quartz (SiO_2), without the presence of graphite carbon (Fig. 2(b)). It is worth noting that the beam size of our XRD instrument is around 3–5 mm, which is much larger than the typical size of the foraminiferal fossils. Thus, the XRD spectra cover both the phase component of the foraminiferal fossils and matrix minerals. These analyses will be further validated by the following characterizations, such as SEM, EDS and Raman spectra.

With the overall phase composition bearing in mind, we further analyzed the domain-specific morphology and composition of our samples. For the K1 specimen, we first confirmed the chambered structure of the foraminiferal fossils using optical microscopy (Figs. 1(b)–1(d)). However, in the SEM, the mass contrast of the foraminiferal fossils and matrix are quite similar (They both consist of calcite ($CaCO_3$) with a small amount of quartz (SiO_2)). Therefore, the foraminiferal fossils and matrix cannot be distinguished in either the second electron (SE) or backscattered electron (BSE) mode (Fig. 2(d)). Nonetheless, by EDS, we can see the difference between the foraminiferal fossils and the matrix. In a typical K1 sample, all of the Ca, C, Si and O elements can be identified through EDS in everywhere. In the foraminiferal domain, there are shortage of Si elements, indicating that SiO_2 or $CaSiO_3$ are less present in the foraminifera (Figs. 2(d_1)–2(d_4)). This phenomenon can be confirmed by EDS element mapping on several other regions of foraminifera (Fig. S2 in the ESM). The partial presence of Si element in the foraminiferal part is because of the penetration of Si signal from SiO_2 or $CaSiO_3$ in the substrate. Typically, the penetration length of the Si signal in EDS [45, 46] is around 10 μm. Inspection of the distribution of C in the K1 specimen shows some aggregation of C, as indicated by EDS mapping (Figs. S3–S13 in the ESM). While in the K2 specimen, we seldomly found an aggregation of carbon (Figs. 2(f)–2(f5), and Figs. S14 and S15 in the ESM).

Further, we magnified specific areas of interest to study the micro-nano level details of our samples. Firstly, the shell of the foraminifera is inspected by SE mode, showing brick-layer-like morphology of the calcite wall of the foraminifera (Fig. 2(e_2)). Further magnification of the carbon-rich area reveals the delaminated-layered structure of graphite and this feature can be observed in many sites inside the foraminifera (Figs. 2(e) and 2(e_1)). The carbon characteristic will be verified in the later-mentioned Raman spectra. We also found enrichment of the silicon element in the K2 sample through EDS mapping, showing patterns of concentric walls (Fig. 2(f_1)). However, the distribution of Si element on the wall is not continuous but shows scattered patterns. This indicates that quartz is grown into the wall of foraminifera, either in the living foraminifera or through the biomineralization or diagenesis process [47].

The aforementioned inclusion of graphite particles can be further verified by EDS line scanning results (Fig. 2(g)). In the first line across a wall in the foraminifera, we found an abrupt peak of carbon at 150–200 μm, indicating a graphite particle here. At this carbon-rich site, an oxygen deficiency can also be found. At another position (300–350 μm), the enrichment of Si and O and depletion of C and Ca are also found in the EDS line scanning, indicating the inclusion of SiO_2 particles here. The line scanning result corresponds well with EDS mapping of Si (Fig. 2(f_1)). Similar results

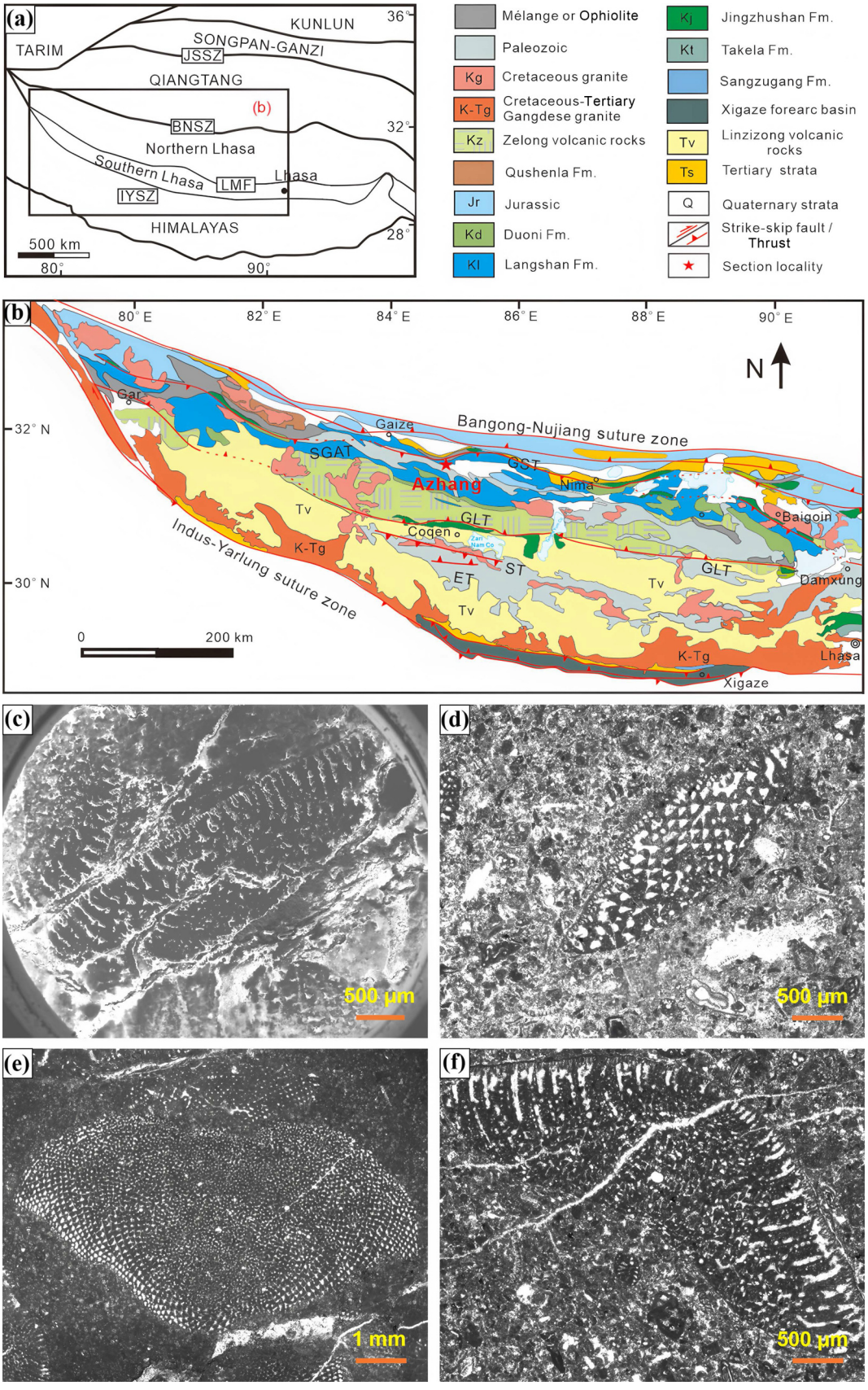

Figure 1 (a) Simplified tectonic map of the Tibetan Plateau and adjacent regions [37]. JSSZ, Jinsha suture zone; BNSZ, Bangong–Nujiang suture zone; LMF, Luobadui–Milashan Fault; IYSZ, Indus–Yarlung suture zone. (b) Simplified geological map of the Lhasa Basin, showing the locality of the Azhang section [37]. GST, Gaize-Selin Co thrust; SGAT, Shiquan–Gaize–Amdo thrust; GLT, Gugu La thrust; ST, Shibaluo thrust; ET, Emei La thrust; Fm., Formation. SEM or optical microscopy images of the (c) and (e) K1 sample, (d) and (f) K2 sample.

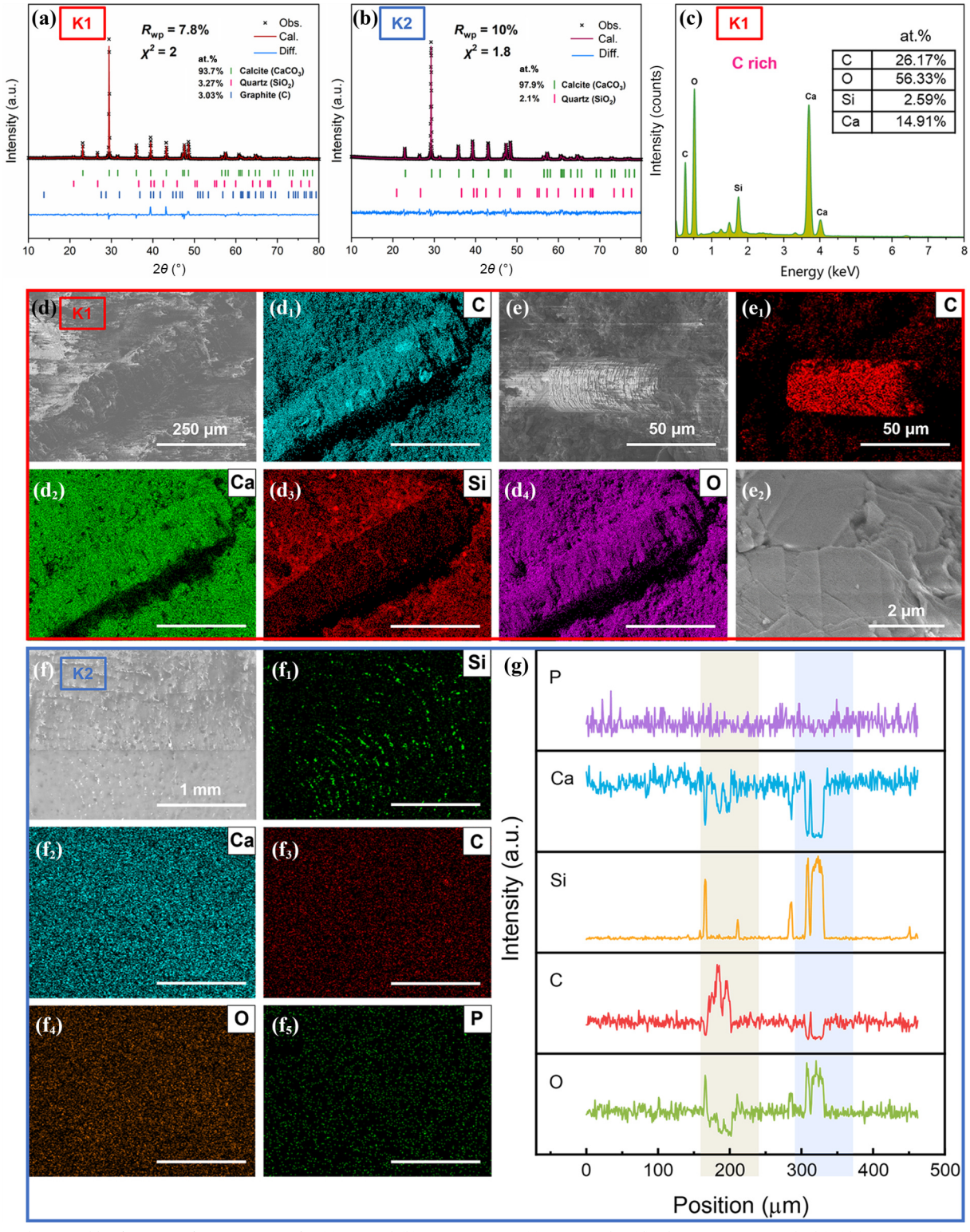

Figure 2 The Rietveld refinement of XRD patterns for (a) K1 and (b) K2 specimens. (c) EDS results. (d) The SEM image, and (d1)–(d4) corresponding element mapping of the K1 specimen. (e) The SEM image of the foraminifera, (e1) the corresponding element mapping and (e2) the localized enlarged view of foraminifera in (e). (f) The SEM image, (f1)–(f5) corresponding element mapping, and (g) EDS line scanning results of the K2 specimen.

can be found elsewhere in this K1 sample (Fig. S12 in the ESM). While for the K2 sample, no enrichment of Carbon element was found even after inspecting several regions of the sample (Figs. S14 and S15 in the ESM). We also performed the transmission electron microscope (TEM) to further investigate the microstructures of the K1 and K2 samples. Figure S18 in the ESM displays low-magnification scaning TEM (STEM) images of the two samples, revealing micrometer-sized grains, pores on the scale of hundreds of nanometers, and a rough morphology. Unfortunately, due to the high sensitivity of the $CaCO_3$-like fossil samples to the electron beam,

we are unable to obtain more detailed microstructural information.

Significantly, we evaluated the energy difference between the unconventional orthorhombic graphite structure observed in this work and the general hexagonal graphite structure based on DFT calculation. The computational results indicate that the orthorhombic graphite structure is energetically unstable compared to the hexagonal counterpart (Fig. 3(a)). We hypothesized that extreme conditions such as volcanic eruptions, lightning strikes, or meteorite impacts could have facilitated the formation of this unconventional metastable graphite structure. We further used site-specific Raman spectroscopy characterization to reveal the spatial distribution of the aforementioned inorganic crystallites. We first need to clarify the typical Raman peaks of calcite ($CaCO_3$), quartz (SiO_2) and graphite (C). For the K1 sample, the peaks of calcite ($CaCO_3$), quartz (SiO_2) and graphite (C) all can be indexed in many sites (Figs. 3(b) and 3(c), and Fig. S19 in the ESM). While for the K2 sample, only calcite ($CaCO_3$) and quartz are frequently found, with a rare appearance of graphite peak (Figs. 3(d) and 3(e), and Fig. S20 in the ESM). The detailed analyses and index of every peak are discussed as follows.

The Raman spectrum of $CaCO_3$ involves the following characteristic peaks and corresponding vibrational modes:

1. A_{1g} mode (located at about 1085 cm^{-1}).

This mode is an in-plane vibration of CO_3 polyhedra and usually shows up as the strongest and sharpest peak in the Raman spectrum. Since this vibration does not involve atoms other than carbonate, it is less sensitive to changes in cation size and nearest neighbor distance (M–O).

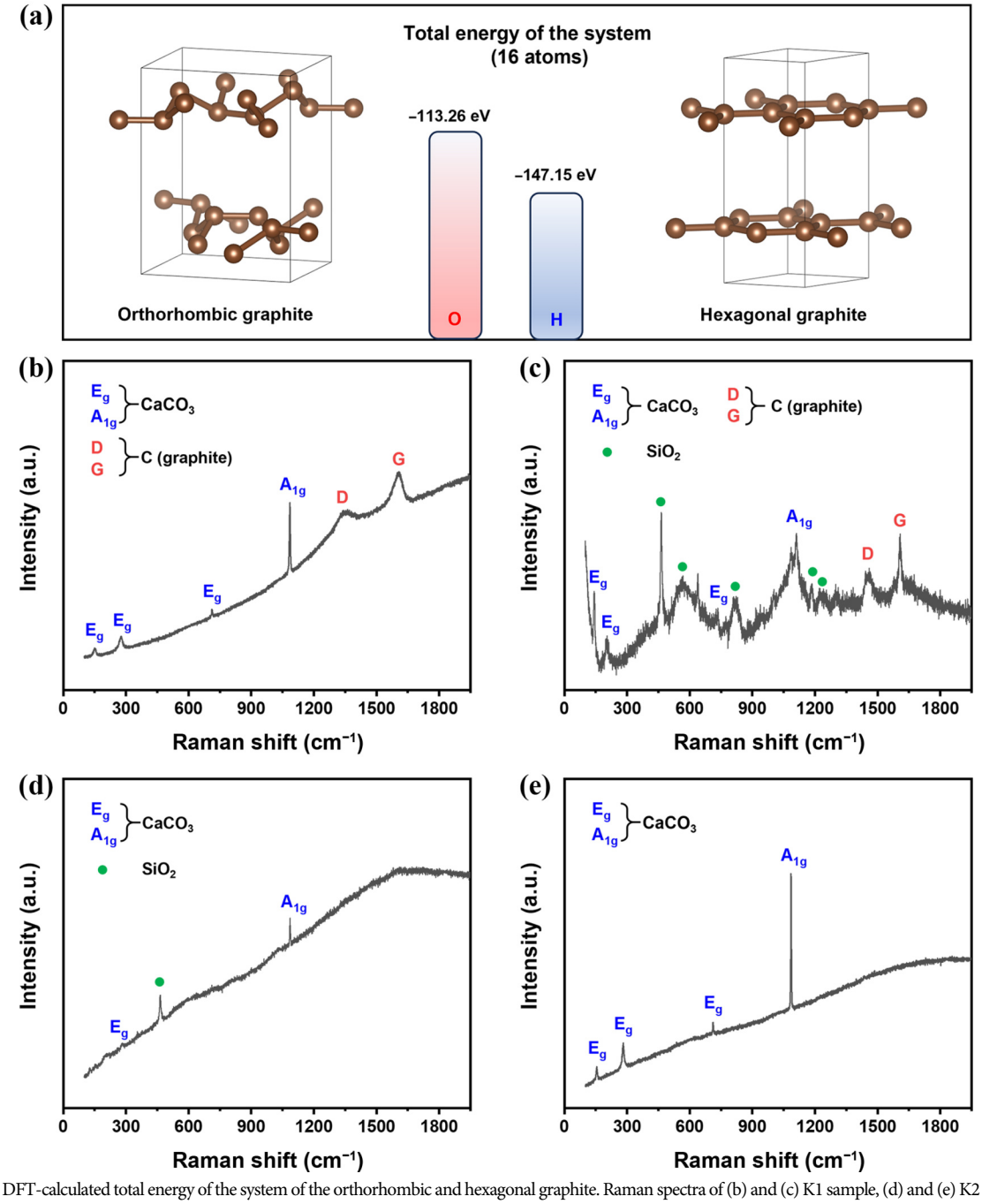

Figure 3 (a) DFT-calculated total energy of the system of the orthorhombic and hexagonal graphite. Raman spectra of (b) and (c) K1 sample, (d) and (e) K2 sample.

2. E_g (internal) mode (located at about 711 and 1434 cm^{-1}).

These modes involve vibrations within the CO_3 polyhedra and usually appear at high relative wave numbers in Raman spectra. These vibrational modes are related to the geometry and chemical bonding of the carbonate.

3. E_g (external) mode (located at about 154 and 281 cm^{-1}).

These modes have lower relative wave numbers in Raman spectra and are more structure-specific.

These modes involve translational (T) and libration (L) vibrations of CO_3 polyhedra in the original unit cell. In particular, the translational (T) mode is very sensitive to changes in the radius of the cation.

4. $E_g + A_{1g}$ combination band (occurs at about 1747 cm^{-1}).

This is produced by the combined vibrations of the E_g and A_{1g} modes and occurs in the region of relatively high wave numbers.

For quartz (SiO_2), the main characteristic peaks in the Raman spectrum are usually associated with the vibrational modes of the Si–O bond. These vibrational modes include symmetric and asymmetric stretching vibrations as well as bending vibrations.

Common characteristic peak positions include:

Approximately 400–470 cm^{-1}: associated with Si–O bending vibrations.

Approximately 800–1200 cm^{-1}: associated with symmetric and asymmetric stretching vibrations of Si–O.

Potential causes of shifted Raman peak positions in SiO_2:

1. Temperature changes.

An increase or decrease in temperature affects the vibrational frequency of the Si–O bonds in silica crystals, resulting in a shift in the position of the Raman peak. This shift is usually characterized by a negative temperature coefficient, i.e., as the temperature increases, the vibrational frequency decreases, and the Raman peak shifts to a lower wave number.

2. Pressure changes.

Changes in external pressure can lead to compression or expansion of the SiO_2 crystal structure, altering the length and angle of the Si–O bonds and thus affecting the position of the Raman peaks. Under high pressure, the Si–O bonds may be compressed, leading to an increase in the vibrational frequency and a shift of the Raman peak towards higher wave numbers.

3. Crystal structure change.

Crystal structure changes in SiO_2, such as a shift from α-quartz to β-quartz, result in a change in the position of the Raman peaks. This structural shift is usually accompanied by changes in bond lengths and bond angles, which affect the vibrational modes and the positions of the Raman peaks.

4. Chemical environment changes.

Chemical modifications on the SiO_2 surface or the presence of adsorbed species may alter the local chemical environment of the Si-O bond and affect its vibrational properties. For example, adsorbed moisture or other polar molecules on the surface may affect the vibration of the Si–O bond through interactions such as hydrogen bonding, resulting in a shift in the Raman peak position.

5. Amorphous vs. crystalline transition.

When SiO_2 transforms from a crystalline state to an amorphous state (e.g., glassy state), the orderliness of its structure decreases, resulting in the broadening and positional changes of the Raman peaks. The Raman peaks of amorphous SiO_2 are usually wider and shifted in position than those of crystalline SiO_2.

6. Stresses and defects.

Stresses and defects within the crystal can also affect the vibrational properties of the Si–O bond, resulting in a shift in the position of the Raman peak. Stresses can be internal (e.g., due to defects during crystal growth) or externally applied (e.g., mechanical stresses).

The Raman spectrum of graphite (C) has the following characteristic peaks and corresponding vibrational modes [48, 49]:

1. D band (defect peak): The D band appears at about 1350 cm^{-1} and is associated with defects and disordered structures in graphite. In particular, it is associated with the vibrational modes of the carbon atoms at the edges of the graphite lattice or defects with A_{1g} symmetry. This peak is more pronounced in highly disordered carbon materials, such as graphene edges or carbon materials with many defects.

2. G band (graph band peak): The G band appears at about 1580 cm^{-1} and is associated with the planar vibrational modes of the sp^2 hybridized carbon atoms in graphite with E_{2g} symmetry. This peak is usually associated with an ordered arrangement of carbon atoms in graphite and is Raman active as it involves a change in the symmetry of the lattice.

Analysis of the D and G peaks

1. Intensity ratio of the D and G peaks (I_D/I_G).

This ratio can be used to assess the degree of disorder in a sample. In highly ordered graphene, the intensity of the G peak is much greater than that of the D peak, whereas in graphene with more disorder or edge regions, the intensity of the D peak will increase relatively.

2. Half peak width of G peak.

The full width at half maximum (FWHM) of the G peak can provide information about the degree of ordering of the carbon atoms in a sample. A wider G-peak usually indicates more disorder or a smaller grain size in the sample.

3. Location of the G peak.

The position of the G-peak may vary depending on the stress state of the sample, hydrogen content, local environment, and other factors. For example, stress can cause the position of the G peak to change.

4. Position of the D peak.

The position of the D peak may also be affected by the distribution of stress and defects in the sample. In some cases, changes in the position of the D peak can provide information about the type of defects in the sample.

5. Resonance effects in Raman spectroscopy.

Resonance effects in Raman spectroscopy can affect the intensity and shape of the D and G peaks. This effect is related to the electronic structure of the sample and the optical excitation process, so the wavelength of the excitation light needs to be taken into account in the analysis.

Theoretically, to understand the atomic vibration information of orthorhombic graphite structures, we computed its phonon dispersion relations, as shown in Fig. S21 in the ESM. The severe imaginary frequencies in the phonon spectrum of the orthorhombic graphite structure primarily stem from the phase's inherent instability. At present, there is little research on the theoretical calculation of such unconventional structure, which poses a huge challenge to our work. Additionally, inaccuracies in computational settings, such as the choice of exchange-correlation functionals and basis sets, along with the sensitivity to thermodynamic conditions, can introduce substantial distortions and energetically unfavorable states, resulting in the observed imaginary frequencies.

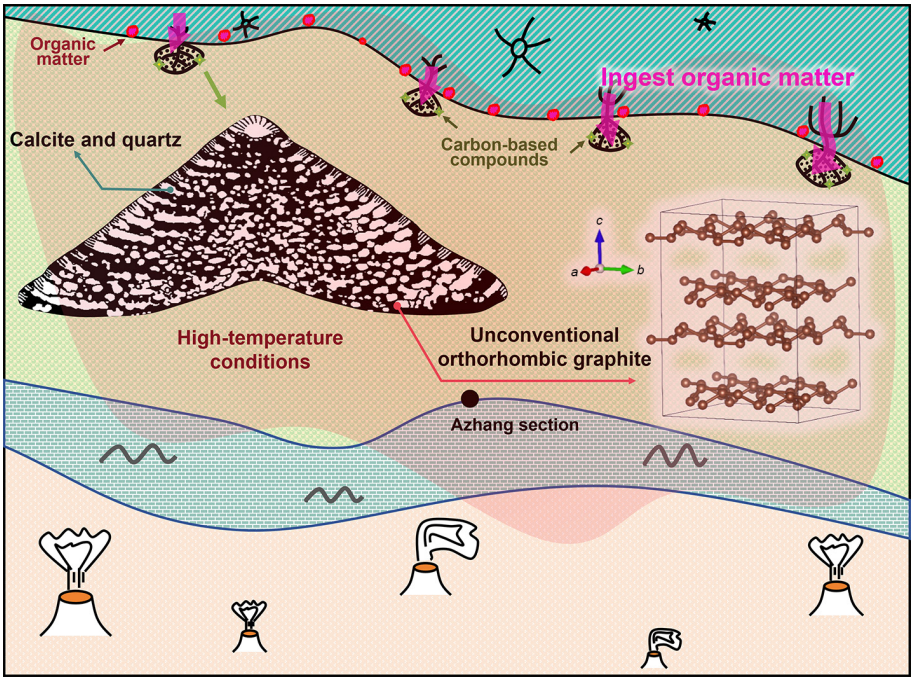

Figure 4 Schematic illustration showing how the ingestion of organic matter and high-temperature environments promote graphitization in foraminifera.

4 Conclusions

We conducted comprehensive characterizations on two sets of Cretaceous foraminifers. First, we used an optical microscope and SEM to observe the morphology. Second, phase components of the inorganic crystallites are analyzed through XRD, and unconventional orthorhombic graphite was found. The energetic landscape and formation mechanism are simulated using DFT. Then, microstructures and micro compositions are revealed by SEM and EDS. Both the EDS line scanning and mapping confirmed the aggregation of graphite and quartz particles. Furthermore, Raman spectra confirmed calcite, quartz and graphite, validating the site of graphite inside the chamberlet of foraminifera. The finding of the unconventional phase of graphite points to high-temperature and/or high-pressure geological events during the mid-Cretaceous (Fig. 4). The current study may inspire materials scientists seeking the unconventional phase of carbon allotropes through learning from nature.

Electronic Supplementary Material: Supplementary material (XRD, SEM and Raman spectroscopy measurements and results) is available in the online version of this article at https://doi.org/10.26599/NR.2025.94907262.

Data availability

All data needed to support the conclusions in the paper are presented in the manuscript and the ESM. Additional data related to this paper may be requested from the corresponding author upon request.

Acknowledgement

We deeply appreciate the meaningful discussions provided by Zhang yichuan, Li Jianguo, and Miao Lanyun. This work is supported by the National Natural Science Foundation of China (Nos. 42293280 and 42472045), the Second Tibetan Plateau Scientific Expedition and Research (No. 2019QZKK0706), and the Natural Science Foundation of Jiangsu Province (No. BK20171102).

Declaration of competing interest

All the contributing authors report no conflict of interests in this work.

Author contribution statement

Q. Y. S.: Data curation, project administration, validation, writing manuscript, experimental design, funding acquisition. Y. W. X.: Data curation, writing manuscript. All the authors have approved the final manuscript.

Use of AI statement

None.

References

[1] Flannery-Sutherland, J. T.; Silvestro, D.; Benton, M. J. Global diversity dynamics in the fossil record are regionally heterogeneous. *Nat. Commun.* **2022**, *13*, 2751.

[2] Agiadi, K.; Hohmann, N.; Gliozzi, E.; Thivaiou, D.; Bosellini, F. R.; Taviani, M.; Bianucci, G.; Collareta, A.; Londeix, L.; Faranda, C. et al. The marine biodiversity impact of the Late Miocene Mediterranean salinity crisis. *Science* **2024**, *385*, 986–991.

[3] Sforna, M. C.; Loron, C. C.; Demoulin, C. F.; François, C.; Cornet, Y.; Lara, Y. J.; Grolimund, D.; Ferreira Sanchez, D.; Medjoubi, K.; Somogyi, A. et al. Intracellular bound chlorophyll residues identify 1 Gyr-old fossils as eukaryotic algae. *Nat. Commun.* **2022**, *13*, 146.

[4] Bernard, S.; Daval, D.; Ackerer, P.; Pont, S.; Meibom, A. Burial-induced oxygen-isotope re-equilibration of fossil foraminifera explains ocean paleotemperature paradoxes. *Nat. Commun.* **2017**, *8*, 1134.

[5] Morard, R.; Hassenrück, C.; Greco, M.; Fernandez-Guerra, A.;

Rigaud, S.; Douady, C. J.; Kucera, M. Renewal of planktonic foraminifera diversity after the Cretaceous Paleogene mass extinction by benthic colonizers. *Nat. Commun.* **2022**, *13*, 7135.

[6] Cisneros-Lazaro, D.; Adams, A.; Guo, J. M.; Bernard, S.; Baumgartner, L. P.; Daval, D.; Baronnet, A.; Grauby, O.; Vennemann, T.; Stolarski, J. et al. Fast and pervasive diagenetic isotope exchange in foraminifera tests is species-dependent. *Nat. Commun.* **2022**, *13*, 113.

[7] Hua, H.; Chen, Z.; Yuan, X. L.; Xiao, S. H.; Cai, Y. P. The earliest Foraminifera from southern Shaanxi, China. *Sci. China Earth Sci.* **2010**, *53*, 1756–1764.

[8] Kryza, R.; Zalasiewicz, J.; Rodionov, N. Enigmatic sedimentary–volcanic successions in the central European Variscides: A Cambrian/Early Ordovician age for the Wojcieszów Limestone (Kaczawa Mountains, SW Poland) indicated by SHRIMP dating of volcanic zircons. *Geol. J.* **2008**, *43*, 415–430.

[9] Dubicka, Z.; Gajewska, M.; Kozłowski, W.; Hallock, P.; Hohenegger, J. Photosynthetic activity in Devonian Foraminifera. *Biogeosciences* **2021**, *18*, 5719–5728.

[10] Chaabane, S.; de Garidel-Thoron, T.; Meilland, J.; Sulpis, O.; Chalk, T. B.; Brummer, G. J. A.; Mortyn, P. G.; Giraud, X.; Howa, H.; Casajus, N. et al. Migrating is not enough for modern planktonic foraminifera in a changing ocean. *Nature* **2024**, *636*, 390–396.

[11] Rosa Marín, A. Benthic foraminifera as bioindicators of coral reef health. *Nat. Rev. Earth Environ.* **2023**, *4*, 733–733.

[12] Adebayo, M. B.; Bolton, C. T.; Marchant, R.; Bassinot, F.; Conrod, S.; de Garidel-Thoron, T. Environmental controls of size distribution of modern planktonic foraminifera in the tropical Indian Ocean. *Geochem., Geophys., Geosyst.* **2023**, *24*, e2022GC010586.

[13] BouDagher-Fadel, M. K. Evolution, extinction, homology and homoplasy of the larger benthic foraminifera from the Carboniferous to the present day, as exemplified by planispiral-fusiform and discoidal forms. *J. Earth Sci.* **2022**, *33*, 1348–1361.

[14] Dubicka, Z.; Gajewska, M.; Kozłowski, W.; Mikhalevich, V. Test structure in some pioneer multichambered Paleozoic foraminifera. *Proc. Natl. Acad. Sci. USA* **2021**, *118*, e2100656118.

[15] Shi, Y. K.; Huang, H.; Shen, Z. H. New insights for ancient foraminifera through 3D visuals of fusulinids. *Palaeoworld* **2019**, *28*, 478–486.

[16] Jenkyns, H. C. Geochemistry of oceanic anoxic events. *Geochem., Geophys., Geosyst.* **2010**, *11*, Q03004.

[17] Ma, Z. T.; Wang, Q. Y.; Liu, L. M.; Zhang, R. A.; Liu, Q. C.; Liu, P. G.; Wu, L. H.; Liu, C. Y.; Bai, Y.; Zhang, Y. D. et al. Low-coordination environment design of single Co atoms for efficient CO_2 photoreduction. *Nano Res.* **2024**, *17*, 3745–3751.

[18] Chen, X.; Liu, Y.; Wang, G. Q.; Kuang, Y. B.; Xiang, X. Q.; Di, G. R.; Yin, X. J.; Zhang, L.; Wang, K. X.; Cai, Q. Q. et al. Recent advances in photocatalytic CO_2 cycloaddition reaction. *Nano Res.* **2024**, *17*, 9601–9619.

[19] Chen, L. L.; Li, M. H.; Zhang, J. N. Tailoring microenvironment for efficient CO_2 electroreduction through nanoconfinement strategy. *Nano Res.* **2024**, *17*, 7880–7899.

[20] Liu, W.; Li, H. Q.; Ou, P. F.; Mao, J.; Han, L. L.; Song, J.; Luo, J.; Xin, H. L. Isolated Cu–Sn diatomic sites for enhanced electroreduction of CO_2 to CO. *Nano Res.* **2023**, *16*, 8729–8736.

[21] Jia, Y. J.; Zhang, Y. D.; Lin, M. Q.; Cheng, Y. Y.; Xu, Y. J. The configuration of $Au^{\delta+}$–$ZrO_2^{\delta-}$ species induced activation enhances electrocatalytic CO_2 to formate conversion. *Nano Res.* **2024**, *17*, 6006–6015.

[22] Li, T.; Zhang, Z. Y.; Luo, D. C.; Xu, B. Y.; Zhang, R. J.; Yao, J. L.; Li, D.; Xie, T. Highly efficient photo-thermal synergistic catalysis of CO_2 methanation over $La_{1-x}Ce_xNiO_3$ perovskite-catalyst. *Nano Res.* **2024**, *17*, 7945–7956.

[23] Guo, H. M.; Wu, L.; Nie, S. Y.; Yang, D. R.; Wang, X. Ultrathin zirconium-porphyrin based nanobelts as photo-coupled electrocatalysis for CH_4 oxidation to CO. *Nano Res.* **2023**, *16*, 12641–12646.

[24] Lv, J.; Wang, Y. H.; Liu, J. J.; Zhang, Z. C.; Ma, Y.; Zhou, Z. Y.; Ouyang, Y. Q.; Zhong, J.; Rao, X.; Sun, H. M. et al. Dry-gel synthesis of hierarchical Ni–La@S-1 catalysts with stabilized Ni–La bimetals nanoparticles for dry reforming of methane. *Nano Res.* **2024**, *17*, 10216–10226.

[25] Gupta, N. S.; Briggs, D. E. G.; Collinson, M. E.; Evershed, R. P.; Michels, R.; Jack, K. S.; Pancost, R. D. Evidence for the *in situ* polymerisation of labile aliphatic organic compounds during the preservation of fossil leaves: Implications for organic matter preservation. *Org. Geochem.* **2007**, *38*, 499–522.

[26] Dutta, S.; Mehrotra, R. C.; Paul, S.; Tiwari, R. P.; Bhattacharya, S.; Srivastava, G.; Ralte, V. Z.; Zoramthara, C. Remarkable preservation of terpenoids and record of volatile signalling in plant-animal interactions from Miocene amber. *Sci. Rep.* **2017**, *7*, 10940.

[27] Marvin, U. B.; Walker, D. A transient heating event in the history of a highlands troctolite from Apollo 12 soil 12033. *J. Geophys. Res.: Solid Earth* **1985**, *90*, C421–C429.

[28] Manning, P. L.; Edwards, N. P.; Bergmann, U.; Anné, J.; Sellers, W. I.; van Veelen, A.; Sokaras, D.; Egerton, V. M.; Alonso-Mori, R.; Ignatyev, K. et al. Pheomelanin pigment remnants mapped in fossils of an extinct mammal. *Nat. Commun.* **2019**, *10*, 2250.

[29] Johnson, P. G. The nearest stellar wind bubble or fossil supernova remnant. *Astrophys. Space Sci.* **1982**, *82*, 213–221.

[30] Blöchl, P. E. Projector augmented-wave method. *Phys. Rev. B* **1994**, *50*, 17953–17979.

[31] Perdew, J. P.; Burke, K.; Ernzerhof, M. Generalized gradient approximation made simple. *Phys. Rev. Lett.* **1996**, *77*, 3865–3868.

[32] BouDagher-Fadel, M.; Price, G. D. Global evolution and paleogeographic distribution of mid-Cretaceous orbitolinids. *UCL Open: Environ.* **2019**, *1*, e001.

[33] Xu, Y. W.; Hu, X. M.; BouDagher-Fadel, M. K.; Sun, G. Y.; Lai, W.; Li, J.; Zhang, S. J. The major Late Albian transgressive event recorded in the epeiric platform of the Langshan Formation in central Tibet. *Geol. Soc. Spec. Publ.* **2020**, *498*, 211–232.

[34] Xu, Y. W.; Hu, X. M.; Garzanti, E.; BouDagher-Fadel, M.; Sun, G. Y.; Lai, W.; Zhang, S. J. Mid-Cretaceous thick carbonate accumulation in Northern Lhasa (Tibet): Eustatic vs. *tectonic control? Geol. Soc. Am. Bull.* **2022**, *134*, 389–404.

[35] Rao, X.; Skelton, P. W.; Sha, J. G.; Cai, H. W.; Iba, Y. Mid-Cretaceous rudists (Bivalvia: Hippuritida) from the Langshan Formation, Lhasa block, Tibet. *Pap. Palaeontol.* **2015**, *1*, 401–424.

[36] BouDagher-Fadel, M. K.; Hu, X. M.; Price, G. D.; Sun, G. Y.; Wang, J. G.; An, W. Foraminiferal biostratigraphy and palaeoenvironmental analysis of the mid-Cretaceous limestones in the southern Tibetan Plateau. *J. Foraminiferal Res.* **2017**, *47*, 188–207.

[37] Pan, G. T.; Ding, J.; Yao, D. S.; Wang, L. Q. Guide Book of 1:1,500,000 Geologic Map of the Qinghai-Xizang (Tibet) Plateau and Adjacent Areas; Cartographic Publishing House: Chengdu, 2004.

[38] Bunaciu, A. A.; Udriştioiu, E. G.; Aboul-Enein, H. Y. X-ray diffraction: Instrumentation and applications. *Crit. Rev. Anal. Chem.* **2015**, *45*, 289–299.

[39] Sakata, M.; Cooper, M. J. An analysis of the Rietveld refinement method. *J. Appl. Crystallogr.* **1979**, *12*, 554–563.

[40] Zeitler, T. R.; Toby, B. H. Parallel processing for Rietveld refinement. *J. Appl. Crystallogr.* **2002**, *35*, 191–195.

[41] Doebelin, N.; Kleeberg, R. *Profex*: A graphical user interface for the Rietveld refinement program *BGMN*. *J. Appl. Crystallogr.* **2015**, *48*, 1573–1580.

[42] Zolotoyabko, E.; Caspi, E. N.; Fieramosca, J. S.; Von Dreele, R. B.; Marin, F.; Mor, G.; Addadi, L.; Weiner, S.; Politi, Y. Differences between Bond Lengths in Biogenic and Geological Calcite. *Cryst. Growth Des.* **2010**, *10*, 1207–1214.

[43] Xie, J.; Zhang, L.; Xing, H. Y.; Bai, P. H.; Liu, B.; Wang, C. J.; Lei, K.; Wang, H.; Peng, S.; Yang, S. Gas sensing of ordered and

disordered structure SiO_2 and their adsorption behavior based on Quartz Crystal Microbalance. *Sens. Actuators B: Chem.* **2020**, *305*, 127479.

[44] Fayos, J. Possible 3D Carbon Structures as Progressive Intermediates in Graphite to Diamond Phase Transition. *J. Solid State Chem.* **1999**, *148*, 278–285.

[45] Newbury, D. E.; Ritchie, N. W. M. Performing elemental microanalysis with high accuracy and high precision by scanning electron microscopy/silicon drift detector energy-dispersive X-ray spectrometry (SEM/SDD-EDS). *J. Mater. Sci.* **2015**, *50*, 493–518.

[46] Goldstein, J. I.; Newbury, D. E.; Michael, J. R.; Ritchie, N. W. M.; Scott, J. H. J.; Joy, D. C. Quantitative analysis: The SEM/EDS elemental microanalysis k-ratio procedure for bulk specimens, step-by-step. In *Scanning Electron Microscopy and X-Ray Microanalysis*. Goldstein, J. I.; Newbury, D. E.; Michael, J. R.; Ritchie, N. W. M.; Scott, J. H. J.; Joy, D. C., Eds.; Springer: New York, 2018; pp 309–339.

[47] Prada, F.; Haramaty, L.; Livnah, O.; Shaul, R.; Abramovich, S.; Mass, T.; Rosenthal, Y.; Falkowski, P. G. Proteomic characterization of a foraminiferal test's organic matrix. *Proc. Natl. Acad. Sci. USA* **2024**, *121*, e2417845121.

[48] Ren, J. K.; Xing, B. Y.; Luo, W.; Luo, B. Y.; Wu, X. F.; Yan, X.; Feng, W. C.; Wang, F. Y.; Cheng, C. J.; Mai, L. Low-temperature-pyrolysis preparation of nanostructured graphite towards rapid potassium storage with high initial Coulombic efficiency. *Nano Res.* **2024**, *17*, 5138–5147.

[49] Zheng, W. J.; Sun, Z. N.; Wang, Y. M.; Xiong, H. M. Fluorescent carbon dots synthesized in solid phase and air for application in LEDs. *Nano Res.* **2024**, *17*, 8495–8503.